

Phonon and magnon Raman scattering in CuB_2O_4

V. G. Ivanov,^{1,*} M. V. Abrashev,¹ N. D. Todorov,¹ V. Tomov,² R. P. Nikolova,³ A. P. Litvinchuk,⁴ and M. N. Iliev⁴

¹*Faculty of Physics, University of Sofia, BG-1164 Sofia, Bulgaria*

²*Institute of Solid State Physics, Bulgarian Academy of Sciences, BG-1184 Sofia, Bulgaria*

³*Institute for Mineralogy and Crystallography, Bulgarian Academy of Sciences, BG-1113 Sofia, Bulgaria*

⁴*Texas Center for Superconductivity, University of Houston, Houston, Texas 77204-5002, USA*

(Received 8 May 2013; revised manuscript received 5 July 2013; published 3 September 2013)

The Brillouin-zone-center phonons and two-magnon excitations in CuB_2O_4 are studied experimentally by polarized Raman spectroscopy. Most of the expected modes are clearly pronounced and their symmetry unambiguously identified from the polarization selection rules. The experimentally observed transverse optical phonon frequencies are in good agreement with those obtained by means of density functional theory. The two-magnon scattering band is centered at 82 cm^{-1} and is clearly identified at temperatures below the Néel temperature T_N . The spectral shape of the two-magnon band confirms the existing theoretical models of magnon dispersion in the commensurate phase of CuB_2O_4 and suggests an exchange integral of $J = 33\text{ cm}^{-1}$ (48 K) between the nearest-neighbor Cu(A) ions. The quantitative line-shape analysis of the two-magnon band evidences for additional magnon self-energy contributions below the temperature T^* of the commensurate-to-incommensurate phase transition.

DOI: [10.1103/PhysRevB.88.094301](https://doi.org/10.1103/PhysRevB.88.094301)

PACS number(s): 78.30.-j, 75.30.Ds, 63.20.dk

I. INTRODUCTION

Copper metaborate (CuB_2O_4) is an intriguing magnetic insulator, which displays several competing spin interactions. Apart from Cu-Cu antiferromagnetic exchange and an easy-plane magnetic anisotropy, relativistic Dzyaloshinskii-Moriya (DM) interactions come into play due to the lack of crystallographic inversion symmetry. That is why CuB_2O_4 is a prototypical system for several important phenomena in physics of magnetically ordered systems. For example, it was the first compound where a static magnetic soliton lattice has been confirmed experimentally.¹ More recently, extraordinary large magneto-optical dichroism² and magneto-electric effect³ have been observed in CuB_2O_4 upon partial substitution of Ni for Cu, which give promise for a wide range of applications in magnetic storage devices and in optoelectronics.

The magnetic phase diagram of CuB_2O_4 has been extensively studied by means of magnetic susceptibility, magnetization, specific heat, and μ -SR measurements⁴ as well as by neutron diffraction.^{1,5} A series of zero-field magnetic phase transitions at temperatures $T_N = 21\text{ K}$ and $T^* = 10\text{ K}$ has been established. The neutron diffraction confirms that at T_N the system undergoes a transition to crystallographically commensurate (C) antiferromagnetic phase existing down to T^* . At lower temperature $T < T^*$, the system exhibits incommensurate (IC) helimagnetic ordering with a propagation vector varying from $\mathbf{q} = (0,0,0)$ at T^* to $(0,0,0.15)$ at 1.8 K. To be more precise, the commensurate phase possesses a weak ferromagnetic moment, which results from a small canting of the neighboring spins from the ideal antiparallel orientation. The presence of two magnetic subsystems, Cu(A) and Cu(B) with magnetic moments of $\approx 0.86\mu_B$ and $0.20\mu_B$, respectively,⁵ is also an important factor driving the C-IC phase transition.^{6,7}

Study of the spin-wave excitations (magnons) is also a valuable tool toward understanding the interplay between exchange interactions, magnetic anisotropy, and DM inter-

actions. The magnon dispersion curves in the commensurate antiferromagnetic phase of CuB_2O_4 , along directions of high symmetry $(0,0,q)$, $(q,q,0)$, and (q,q,q) , has been examined by means of inelastic neutron scattering (INS).^{8,9} Measurements confirm the existence of two-magnon branches, which stem from the two magnetic sublattices. The maximum magnon energies for the Cu(A) sublattice reach 8 meV, while for the Cu(B) sublattice they do not exceed 2 meV.

A logical further step toward unraveling the physics of magnetic ordering in CuB_2O_4 would be to explore the evolution of the magnon spectra below the transition temperature T^* for the C-IC phase transition. In this work, we address this problem by identifying and inspecting the two-magnon light scattering band in the Raman spectra of copper metaborate at temperatures ranging from 180 down to 4 K. According to INS measurements, the two-magnon excitation spectrum of the Cu(A) sublattice should extend approximately to 16 meV, or 130 cm^{-1} , which falls into the accessible spectral range of present day Raman spectrometers.

The identification of the two-magnon band inevitably relies on the assignment of the numerous Γ -point phonons abundant in the Raman spectra of CuB_2O_4 . To the best of our knowledge, no previous study addresses optical phonons in copper metaborate, and our work aims also at filling this gap. We assign the optical phonons on the basis of a careful comparison of the experimentally observed Raman frequencies and polarization selection rules with the results of the factor-group analysis and *ab initio* density functional theory (DFT) calculations of the normal vibrations in CuB_2O_4 .

The paper is organized as follows. A detailed description of the samples' synthesis and their x-ray characterization, the Raman experimental setups, and the methods of calculation is given in Sec. II; Sec. III presents the experimental Raman spectra and their theoretical interpretation. Section IV summarizes the main results and conclusions of the work.

II. SAMPLES, EXPERIMENTAL SETUPS, AND CALCULATION DETAILS

CuB₂O₄ single crystals were successfully grown by the high-temperature solution growth method. The starting materials CuO and B₂O₃ were taken in 1:20 molar ratio, B₂O₃ being used as a flux. The mixture of materials was first homogenized for 48 h at 980 °C and then cooled to 750 °C at a cooling rate of 1 °C/h. The crystals were grown in a platinum crucible and the process took place in a resistive heating oven in air atmosphere. The size of the crystals synthesized at the bottom and walls of the crucible was up to 7 × 3 × 3 mm³.

The crystallographic characterization of the crystals was carried out by x-ray single-crystal diffractometry. A single crystal was mounted on a glass capillary and diffraction data were collected at room temperature by an ω -scan technique, on an Agilent Diffraction SuperNova dual four-circle diffractometer equipped with an Atlas CCD detector. A mirror-monochromatized Mo K_{α} radiation from a microfocus source was used ($\lambda = 0.7107$ Å). The determination of the cell parameters, data integration, scaling, and absorption correction were carried out using the program package CRYCALISPRO.¹⁰ The structure was solved by direct methods (SHELXS-97) (Ref. 11) and refined by full-matrix least-square procedures on F^2 . The single-crystal x-ray diffraction confirmed the $I\bar{4}2d$ crystal structure with lattice parameters $a = 11.4972$ Å and $c = 5.6290$ Å and atomic site positions close to those of Refs. 12 and 13.

The Raman measurements at room temperature were carried out using micro-Raman spectrometer LabRAM HR800 Visible. An objective ×50 was used both to focus the incident laser beam and to collect the scattered light. To check the presence of resonance effects in the Raman spectra, He-Ne (633 nm, 1.96 eV) and Ar⁺ [515 nm (2.41 eV), 488 nm (2.54 eV), and 458 nm (2.71 eV)] lasers were used as excitation sources. The Raman spectra at low temperatures were obtained using triple T64000 micro-Raman spectrometer and Oxford Instruments liquid helium flow cryostat.

The first-principles calculations of the electronic ground state were performed within the generalized-gradient approximation (GGA) with Perdew-Burke-Ernzerhof¹⁴ local functional using the CASTEP code.¹⁵ Ultrasoft pseudopotentials were used. For self-consistent calculations of the electronic structure, the integration over the Brillouin zone was performed over the 5 × 5 × 3 Monkhorst-Pack grid in the reciprocal space.¹⁶ A lattice relaxation has been performed until forces on atoms did not exceed 10 meV/Å. After that, the lattice dynamics was calculated by the finite displacements method.¹⁷ This approach does not allow us to evaluate the electric field response and calculate nonanalytical corrections to longitudinal optical (LO) phonon frequencies.

III. RESULTS AND DISCUSSION

A. Phonon scattering

Copper metaborate possesses a relatively large unit cell for its simple chemical formula and, consequently, a large number of Γ -point phonons. The copper and boron atoms occupy two sets of Wyckoff positions, whereas the oxygen atoms are distributed among four sets of Wyckoff positions, as shown

TABLE I. Wyckoff position of the atoms in the unit cell of CuB₂O₄ ($I\bar{4}2d$, No. 122, $Z = 12$). The irreducible representations of the Γ -point phonon modes are $\Gamma_{\text{Total}} = 13A_1 + 17A_2 + 14B_1 + 18B_2 + 32E$ (Ref. 18).

Atom	Wyckoff notation	Irreducible representations
Cu(A)	4b	$B_1 + B_2 + 2E$
Cu(B)	8d	$A_1 + 2A_2 + B_1 + 2B_2 + 3E$
O(1)	16e	$3A_1 + 3A_2 + 3B_1 + 3B_2 + 6E$
O(2)	8d	$A_1 + 2A_2 + B_1 + 2B_2 + 3E$
O(3)	8d	$A_1 + 2A_2 + B_1 + 2B_2 + 3E$
O(4)	16e	$3A_1 + 3A_2 + 3B_1 + 3B_2 + 6E$
B(1)	16e	$3A_1 + 3A_2 + 3B_1 + 3B_2 + 6E$
B(2)	8d	$A_1 + 2A_2 + B_1 + 2B_2 + 3E$
Raman		$13A_1 + 14B_1 + 17B_2 + 31E$
Infrared		$17B_2 + 31E$
Acoustic		$B_2 + E$
Silent		$17A_2$

in Table I. This results in a total number of 75 Raman-active modes, which are classified according to their symmetry as¹⁸

$$\Gamma_{\text{Raman-active}} = 13A_1 + 14B_1 + 17B_2 + 31E \quad (1)$$

with the corresponding Raman tensors

$$A_1 = \begin{pmatrix} a & 0 & 0 \\ 0 & a & 0 \\ 0 & 0 & b \end{pmatrix}, \quad B_1 = \begin{pmatrix} c & 0 & 0 \\ 0 & -c & 0 \\ 0 & 0 & 0 \end{pmatrix},$$

$$B_2(z) = \begin{pmatrix} 0 & d & 0 \\ d & 0 & 0 \\ 0 & 0 & 0 \end{pmatrix}, \quad E(x) = \begin{pmatrix} 0 & 0 & 0 \\ 0 & 0 & e \\ 0 & e & 0 \end{pmatrix},$$

$$E(y) = \begin{pmatrix} 0 & 0 & e \\ 0 & 0 & 0 \\ e & 0 & 0 \end{pmatrix}.$$

Due to the fact that B_2 and E phonons are both Raman and infrared active, TO-LO frequency splitting of these modes can be expected in different scattering configurations. The induced electric dipole moment of B_2 modes is parallel to the [001] crystal direction, whereas the dipole moment of E modes is parallel to the (001) plane.

Our single crystals display elongated shape along the c axis with naturally grown {100} and {001} surfaces. Additionally, narrow {110} surfaces are visible under optical microscope. By inspecting the polarization selection rules from these crystal surfaces, the phonon symmetries can be uniquely identified according to the analysis presented in Table II. The axes x , y , z , x' , and y' are parallel to [100], [010], [001], [110], and $[\bar{1}10]$ crystal directions, respectively.

The polarized room-temperature Raman spectra in all experimentally available scattering configurations are shown in Fig. 1. A large number of phonon lines are observed in the spectral interval between 100 and 1300 cm⁻¹. By following the selection rules given in Table II, we were able to unequivocally assign 12 out of the 13A₁, 11 out of 14B₁, 14 out of the 17B₂, and 18 out of the 31E normal modes. The frequencies of lines belonging to one and the same symmetry are marked with identical colors in Fig. 1. Some of the strongest lines are

TABLE II. Selection rules for the Raman-active modes in a crystal structure of $I\bar{4}2d$ space group in the experimentally available scattering configurations.

(001) surface	$z(xx)\bar{z}$	$z(xy)\bar{z}$	$z(x'x')\bar{z}$	$z(x'y')\bar{z}$
A_1	a^2	0	a^2	0
B_1	c^2	0	0	c^2
B_2	0	$d^2(\text{LO})$	$d^2(\text{LO})$	0
E	0	0	0	0
(010) surface	$y(xx)\bar{y}$	$y(xz)\bar{y}$	$y(zz)\bar{y}$	
A_1	a^2	0	b^2	
B_1	c^2	0	0	
B_2	0	0	0	
E	0	$e^2(\text{LO})$	0	
(110) surface	$y'(x'x')\bar{y}'$	$y'(x'z)\bar{y}'$	$y'(zz)\bar{y}'$	
A_1	a^2	0	b^2	
B_1	0	0	0	
B_2	$d^2(\text{TO})$	0	0	
E	0	$e^2(\text{LO})$	0	

observed also in forbidden scattering configurations, which is ascribed to polarization leakage.

The experimentally observed phonon frequencies are summarized in Table III, and are compared with the results

of DFT normal-mode calculations. Only LO phonons of E symmetry were observed experimentally. For B_2 and E modes, only transverse optical (TO) frequencies were calculated as explained in Sec. II. The close correspondence, within 5%, between the experimental frequencies of the TO modes and the theoretical expectations corroborates the mode assignment based on the polarization selection rules.

In order to exclude the possibility of any photoluminescence contribution, Raman spectra were recorded with four different excitation wavelengths spanning the visible range. Shown in Fig. 2 are the spectra in the $y(zz)\bar{y}$ configuration, where only A_1 phonon lines are allowed. The spectral line positions are identical in different spectra, which proves their Raman origin. Moreover, there is no significant intensity redistribution among the spectral lines upon changing the excitation wavelength. According to optical absorption measurements,¹⁹ the shortest excitation wavelength in our experiment is nearly 100 nm off resonance with the interband gap of CuB_2O_4 . Therefore, no resonant effects in the visible Raman spectra are to be expected in agreement with our results.

B. Two-magnon scattering: Selection rules

Upon lowering the temperature, a broad spectral wing emerges below 150 cm^{-1} , as evident from Fig. 3. It evolves

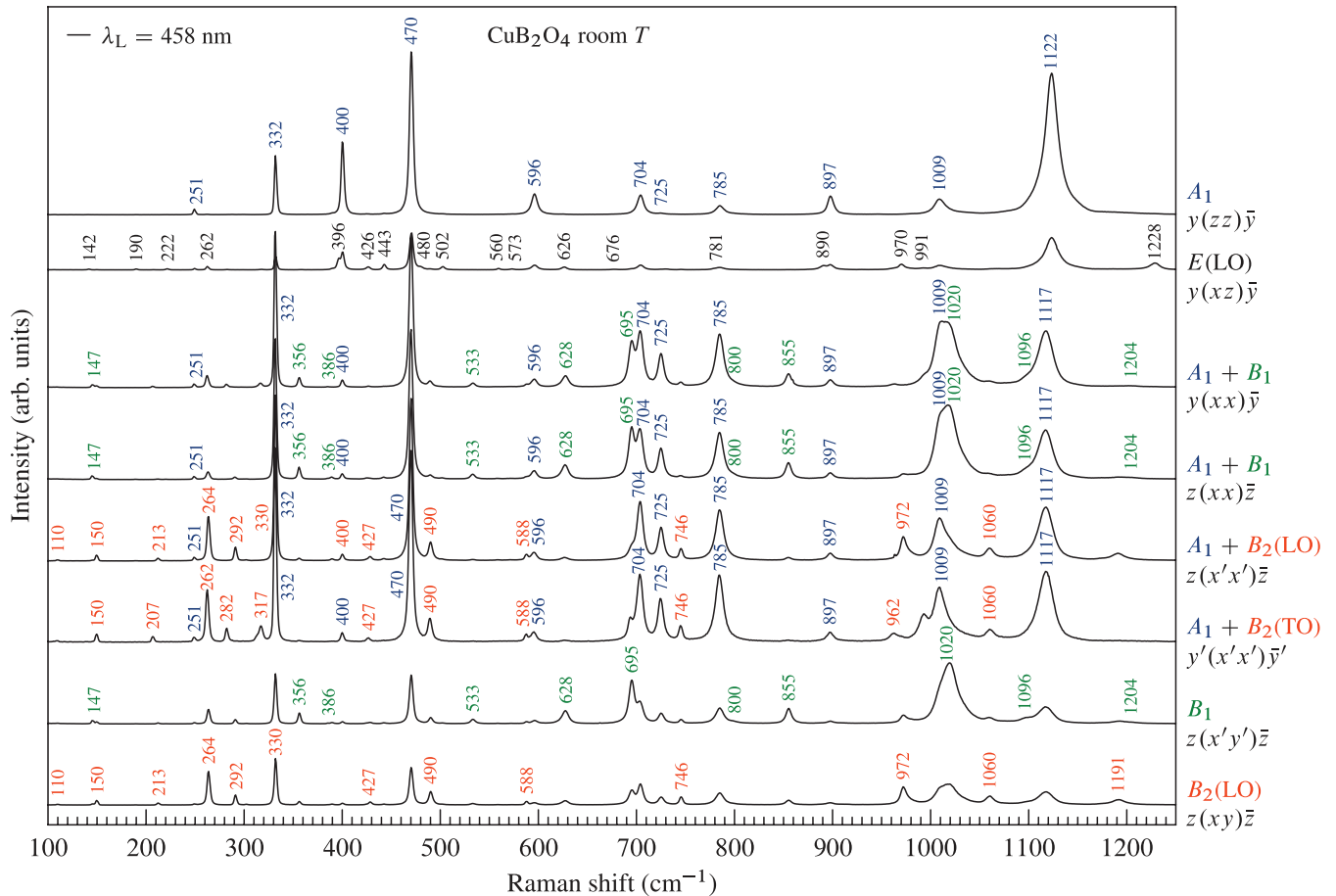


FIG. 1. (Color online) Polarized room-temperature Raman spectra of CuB_2O_4 for 458-nm excitation. Frequencies are shown only for those lines, which are allowed in a given scattering configuration. Raman lines of equivalent symmetries are labeled with one and the same color. The unlabeled lines correspond to polarization leakage from other scattering configurations.

TABLE III. Experimental and calculated frequencies (in cm^{-1}) of Γ -point Raman-active modes in CuB_2O_4 .

A_1		B_1		B_2 (TO/LO)		E (TO/LO)	
Expt.	DFT	Expt.	DFT	Expt.	DFT	Expt.	DFT
251	244	147	127	-/110	123/-	-/142	133/-
332	328	-	242	150/150	131/-	-/-	150/-
400	391	356	337	207/213	200/-	-/190	176/-
470	469	386	380	262/264	216/-	-/222	215/-
596	576	533	504	282/292	245/-	-/262	230/-
704	692	-	583	317/330	313/-	-/-	266/-
725	704	628	604	427/427	408/-	-/-	308/-
785	770	695	692	490/490	465/-	-/-	331/-
-	869	800	775	588/588	566/-	-/396	346/-
897	918	855	833	-/704	679/-	-/426	394/-
1009	952	-	1001	746/746	714/-	-/443	429/-
1117	1048	1020	1015	-/-	847/-	-/480	452/-
1122	1098	1096	1032	-/-	892/-	-/502	466/-
		1204	1091	-/-	920/-	-/560	535/-
				962/972	955/-	-/573	564/-
				1060/1060	974/-	-/626	595/-
				-/1191	1056/-	-/676	669/-
						-/-	725/-
						-/-	768/-
						-/781	774/-
						-/890	861/-
						-/-	891/-
						-/-	903/-
						-/-	923/-
						-/-	941/-
						-/-	963/-
						-/970	966/-
						-/991	988/-
						-/-	1058/-
						-/-	1082/-
						-/1228	1113/-

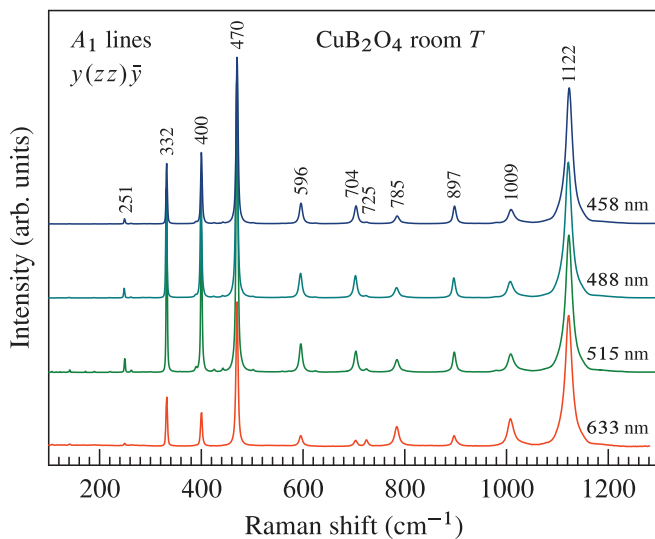


FIG. 2. (Color online) Raman spectra of CuB_2O_4 obtained in $y(zz)\bar{y}$ scattering configuration at 300 K with four different laser lines. Only A_1 lines are allowed in this configuration.

into a broad band centered at 82 cm^{-1} at temperatures below the Néel temperature $T_N = 21 \text{ K}$ of the commensurate (C) magnetic transition. It is seen in Fig. 4 that this band is present with identical line shapes in $xx(yy)$, $x'y'$, and $xz(yz)$ scattering configurations, and is practically missing in zz and $x'x'$, i.e., it corresponds to a mixture of B_1 and E symmetries in the D_{2d} point group. The intensity of the band gradually increases upon lowering the temperature and becomes comparable to the intensity of phonon lines. The spectral position and the width of the band do not show apparent discontinuities near the C-IC transition temperature of 10 K. The correlation of this band with the transition to commensurate phase allows us to hypothesize that it originates primarily from magnetic excitations of the antiferromagnetic ordering.

Generally speaking, two types of magnetic excitations, i.e., one magnon and two magnon, display Raman activity. The mechanisms of the two types of magnetic Raman scattering, however, are quite different and are easy to discriminate experimentally. The one-magnon Raman scattering, in our case, could be ruled out for several arguments. First, the one-magnon scattering is promoted by virtue of spin-orbit

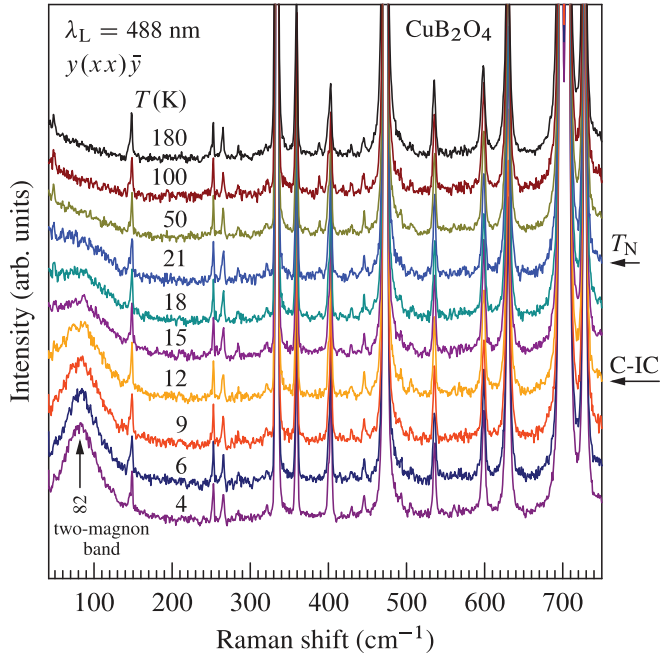


FIG. 3. (Color online) Evolution of the Raman spectra of CuB_2O_4 in $y(xx)\bar{y}$ scattering configuration and 488-nm excitation upon decreasing the temperature from 180 to 4 K.

coupling and gives rise to Raman lines, which are much weaker than the typical phonon bands. Second, as the one-magnon scattering involves only Γ -point excitations, it is characterized by very narrow lines, in contrast to the $\approx 50 \text{ cm}^{-1}$ width of the experimentally observed band. Finally, the frequency of the Γ -point magnons is proportional to the magnetic-anisotropy field H_A . According to electron spin resonance (ESR) measurements⁷ $H_A = 3.9 \text{ T}$ for the Cu(A) ($4b$) sites, which corresponds to a magnon Γ -point energy of $\mu_B H_A = 1.8 \text{ cm}^{-1}$. Obviously, this value is far below the

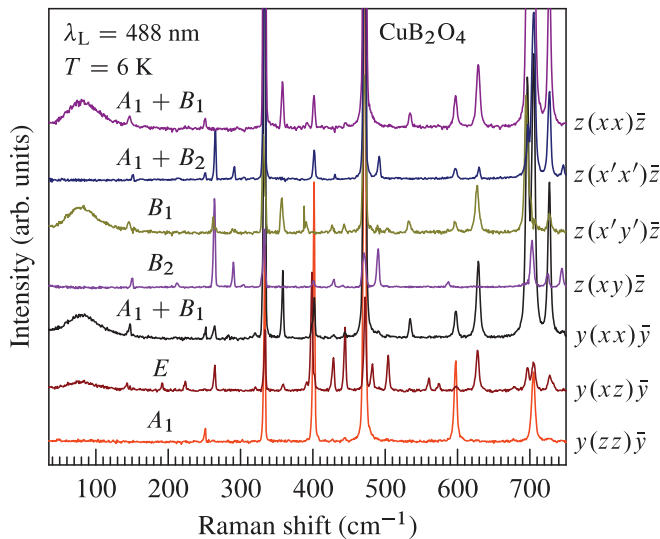


FIG. 4. (Color online) Raman spectra of CuB_2O_4 at 6 K in $z(xx)\bar{z}$, $z(x'x')\bar{z}$, $z(x'y')\bar{z}$, $z(xy)\bar{z}$, $y(xx)\bar{y}$, $y(xz)\bar{y}$, and $y(zz)\bar{y}$ scattering configurations.

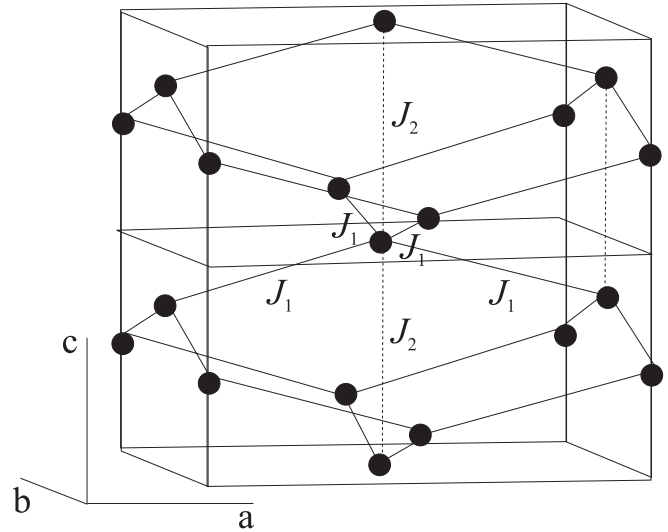


FIG. 5. The sublattice of the Cu(A) ($4b$) positions. Indicated are the strong (J_1) and the weak (J_2) exchange interactions.

energy scale available in the Raman experiments. Therefore, in this section we will provide rigorous arguments in favor of the two-magnon origin of the 82 cm^{-1} band.

The two-magnon Raman scattering is usually manifested by intense and broad bands. According to the Fleury-Loudon (FL) mechanism,²⁰ the two-magnon Raman process consists of a spin exchange between antiferromagnetically interacting ions, proceeding via two consecutive electric dipole transitions. That is why the cross section of the two-magnon scattering is comparable to that of the phonon Raman scattering. The two inequivalent copper positions, Cu(A) ($4b$) and Cu(B) ($8d$), form two weakly interacting magnetic sublattices.⁵ The INS measurements and the theoretical calculations show that the spin-wave excitations in the two subsystems are well decoupled.^{8,9} While the maximum magnon energy in the Cu(B) sublattice is estimated at $\approx 1.5 \text{ meV}$ (12 cm^{-1}), the magnon spectrum of the Cu(A) subsystem is expected to extend up to 8 meV (64 cm^{-1}). Therefore, the band at 82 cm^{-1} falls deeply within the spectral range of the two-magnon excitations of the Cu(A) sublattice.

Shown in Fig. 5 is the Cu(A) sublattice and the relevant exchange interactions between nearest neighbors.⁵ Each Cu(A) ion is antiferromagnetically coupled by a strong exchange $J_1 = k_B \times 45 \text{ K} = 31 \text{ cm}^{-1}$ with four neighbors. The “strong” bonds are parallel to the ac and bc planes, respectively, and are inclined at an angle $\theta \approx \pm 13^\circ$ with respect to the ab plane. Two “weak” bonds of an exchange integral $J_2 = k_B \times 6.5 \text{ K} = 9.4 \text{ cm}^{-1}$ are formed with the two neighbors along the c axis. Additionally, Dzyaloshinskii-Moriya (DM) interaction $\mathbf{D} \cdot (\mathbf{S}_i \times \mathbf{S}_j)$ with $D = k_B \times 2.9 \text{ K} = 4.2 \text{ cm}^{-1}$ is necessary to explain the small inclination ($\approx 3^\circ$) of the neighboring spins from the ideal antiparallel orientation dictated by the J_1 exchange. It is clear from the described hierarchy of interactions that the J_2 exchange and the DM interactions are insignificant for the explanation of the 82 cm^{-1} band. Therefore, we assume that the spectral shape and position of the two-magnon band can be satisfactorily described by the

TABLE IV. Effective Raman Hamiltonians for the two-magnon Raman scattering in different polarization configurations.

Scattering configuration	Effective Raman Hamiltonian
xx	$\cos^2 \theta \sum_i \mathbf{S}_i \cdot \mathbf{S}_{i+d_1}$
xy	0
xz	$\cos \theta \sin \theta \sum_i \mathbf{S}_i \cdot \mathbf{S}_{i+d_1}$
$x'x'$	$\frac{1}{2} \cos^2 \theta \sum_i (\mathbf{S}_i \cdot \mathbf{S}_{i+d_1} + \mathbf{S}_i \cdot \mathbf{S}_{i+d_2})$
$x'y'$	$\frac{1}{2} \cos^2 \theta \sum_i (\mathbf{S}_i \cdot \mathbf{S}_{i+d_1} - \mathbf{S}_i \cdot \mathbf{S}_{i+d_2})$

simplified exchange Hamiltonian

$$H = J_1 \sum_{i,d} \mathbf{S}_i \cdot \mathbf{S}_{i+d}, \quad (2)$$

where the index i runs over the translationally equivalent $00\frac{1}{2}$ positions and the vector \mathbf{d} spans the four possible directions to the set of $0\frac{1}{2}\frac{1}{4}$ neighbors.

By following the FL approach,²⁰ the effective Hamiltonian describing the two-magnon Raman process is

$$H_R \propto \sum_{i,d} (\mathbf{e}_{\text{inc}} \cdot \mathbf{d})(\mathbf{e}_{\text{scatt}} \cdot \mathbf{d}) \mathbf{S}_i \cdot \mathbf{S}_{i+d}, \quad (3)$$

where \mathbf{e}_{inc} and $\mathbf{e}_{\text{scatt}}$ are the polarization vectors of the incident and the scattered photons, respectively. Table IV summarizes the forms of the Raman Hamiltonian for the experimentally available polarization configurations. The polarization directions specified by the unit vectors $\hat{\mathbf{x}}' = 1/\sqrt{2}(\hat{\mathbf{x}} + \hat{\mathbf{y}})$ and $\hat{\mathbf{y}}' = 1/\sqrt{2}(\hat{\mathbf{x}} - \hat{\mathbf{y}})$ are tilted by 45° relative to the axes a and b , respectively. The vectors $\mathbf{d}_1 = \pm \cos \theta \hat{\mathbf{x}} - \sin \theta \hat{\mathbf{z}}$ and $\mathbf{d}_2 = \pm \cos \theta \hat{\mathbf{y}} + \sin \theta \hat{\mathbf{z}}$ specify the “strong” Cu-Cu bonds parallel to the ac and bc planes, respectively.

Although the effective Hamiltonian for the $x'x'$ configuration is nonzero, it commutes with the exchange Hamiltonian (2) and, consequently, does not contribute to inelastic light scattering. Therefore, the FL interaction given by Eq. (3) results in nonvanishing Raman scattering in the $xx(yy)$, $x'y'$, and $xz(yz)$ polarization configurations in full agreement with the experimentally established polarization selection rules for the 82-cm^{-1} band. Moreover, the same type of Raman Hamiltonians correspond to the xx and xz configurations, which corroborates the similar spectral shape of the band in the two configurations.

C. Two-magnon scattering: Line-shape analysis

A decisive piece of evidence for the two-magnon origin of the band at 82 cm^{-1} could be deduced from a detailed analysis of its spectral shape and position. Since the original work of Fleury and Loudon,²⁰ the calculation of spectral shape of the two-magnon Raman scattering has been addressed in several theoretical papers, especially in the context of the high- T_c superconducting (HTS) cuprates.^{21,22} In the latter case, the maximum of the two-magnon band has been calculated at $\omega_0 = 2.78J$. The HTS cuprates are a prototypical example of a quasi-two-dimensional (quasi-2D) $S = \frac{1}{2}$ antiferromagnet on a square lattice. They resemble the Cu(A) sublattice of CuB_2O_4 in two aspects: the $S = \frac{1}{2}$ spin state of the Cu^{2+} ions, and the $Z = 4$ coordination number. It means that the energy cost of a

simultaneous spin reversal of two nearest-neighbor Cu^{2+} ions would scale to the exchange integral J in roughly the same proportion in the two systems. The as-estimated Cu(A)-Cu(A) exchange integral in CuB_2O_4 is $J_1 = 29\text{ cm}^{-1}$, which is in near agreement with the value of 31 cm^{-1} obtained by electron spin resonance (ESR). This analogy, however, does not apply to the line shape of the two-magnon band due to a principal topological difference between the two systems. As seen from Fig. 5, Cu(A) positions in copper metaborate form a system of strongly interconnected planes in contrast to the almost isolated CuO_2 layers in HTS cuprates. As a result, a significant magnon dispersion is present along the crystallographic c axis in CuB_2O_4 as opposed to the practically dispersionless along c magnon branches in HTS cuprates.

By following the results of magnon dispersion calculations,⁸ in the case of negligible magnetic anisotropy and DM interactions, the magnon energy in the Cu(A) subsystem of CuB_2O_4 is given by the equation

$$E(\mathbf{k}) = ZSJ_1 \sqrt{1 - \gamma(\mathbf{k})^2}, \quad (4)$$

where

$$\gamma(\mathbf{k}) = \frac{1}{2} \cos\left(\frac{k_z c}{4}\right) \left[\cos\left(\frac{k_x a}{2}\right) + \cos\left(\frac{k_y a}{2}\right) \right]. \quad (5)$$

In the approximation of noninteracting magnons, the two-magnon scattering intensity is proportional to the imaginary part of the “undressed” Green’s function

$$G_0(\bar{\omega}) = \int_{\text{BZ}} \frac{d^3 \mathbf{k}}{(2\pi)^3} \frac{f(\mathbf{k})^2}{\bar{\omega} - \bar{\Omega}(\mathbf{k}) - i\delta}, \quad (6)$$

where $\bar{\omega} = \omega/\omega_{\text{max}}$ is the Raman shift ω normalized by the high-frequency cutoff $\omega_{\text{max}} = 2ZSJ$ of the two-magnon spectrum, $\bar{\Omega}(\mathbf{k}) = 2E(\mathbf{k})/\omega_{\text{max}}$, and $f(\mathbf{k})$ is a configuration dependent coupling coefficient between the electromagnetic field and the two-magnon excitations. The integration in Eq. (6) is performed over the magnetic Brillouin zone (BZ), which in the case of CuB_2O_4 coincides with the crystallographic BZ. We will determine the coupling coefficient $f(\mathbf{k})$ by transforming the spin operators in the Raman Hamiltonian (3) into momentum representation:

$$\mathbf{S}_i = \int_{\text{BZ}} \frac{d^3 \mathbf{k}}{(2\pi)^3} \exp(i\mathbf{k} \cdot \mathbf{x}_i) \mathbf{S}_{\mathbf{k}}. \quad (7)$$

For a specific scattering configuration, e.g., B_1 , we obtain

$$H_R \propto \int_{\text{BZ}} \frac{d^3 \mathbf{k}}{(2\pi)^3} f(\mathbf{k}) \mathbf{S}_{a,\mathbf{k}} \cdot \mathbf{S}_{b,-\mathbf{k}}, \quad (8)$$

where a and b denote $00\frac{1}{2}$ and $0\frac{1}{2}\frac{1}{4}$ Wyckoff positions, respectively. The coupling coefficient is given by the equation

$$f(\mathbf{k}) = \cos\left(\frac{k_z c}{4}\right) \left[\cos\left(\frac{k_x a}{2}\right) - \cos\left(\frac{k_y a}{2}\right) \right], \quad (9)$$

which differs from the corresponding coupling coefficient for a 2D antiferromagnet by the k_z -dependent cosine prefactor.

As investigated extensively in Refs. 21 and 22, the noninteracting magnon approximation (6) leads to unphysical singularities of the two-magnon spectrum at $\omega = \omega_{\text{max}}$. It is demonstrated that on account of the magnon-magnon interactions, which are especially significant in the $S = \frac{1}{2}$ case,

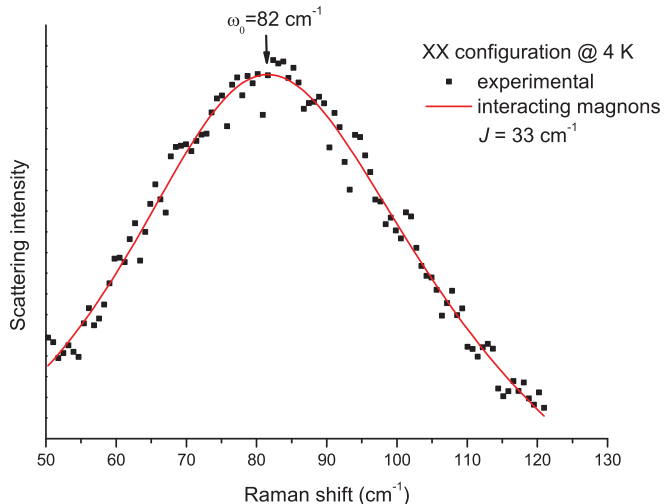


FIG. 6. (Color online) Comparison between the experimental line shape of the two-magnon band at 4 K (dots) and the model of interacting magnons (10) (solid line).

the two-magnon scattering intensity $R(\omega)$ is described by the imaginary part of a renormalized Green's function

$$R(\omega) \propto \text{Im} \left(\frac{G_0(\omega)}{1 + rG_0(\omega)} \right), \quad (10)$$

where r is a dimensionless renormalization coefficient accounting for the magnon self-energy effects. The origin of the magnon self-energy may be twofold. First, an intrinsic “kinematic” interaction, originating from the nonlinear character of the Dyson-Maleev^{23,24} representation of the spin operators, is unavoidably present and is especially significant in the low-spin systems. Second, r may incorporate any additional interaction unaccounted in the simplified exchange Hamiltonian (2).

Instead of calculating r on the basis of a microscopic theory, we will consider it as a phenomenological parameter, which can be estimated by fitting Eq. (10) to the experimental spectra. The nearest-neighbor exchange integral J_1 is also considered as an adjustable parameter. Figure 6 shows the as-fitted two-magnon band at $T = 4$ K in the xx (B_1) scattering configuration. The estimated values of the parameters are $J_1 = 33.1 \pm 0.9$ cm^{-1} and $r = 1.29 \pm 0.03$. The close matching between the theoretical model of interacting magnons and the experimental line shape undoubtedly confirms the two-magnon origin of the 82-cm^{-1} band. Evidently, the estimated exchange integral is in perfect agreement with the experimental results from ESR (Ref. 7) and INS.⁸

The fitted values of J_1 at higher temperatures do not show any systematic temperature dependence and are scattered within estimated confidence intervals. As evident from Fig. 7, however, the estimated values of r decrease steadily upon increasing the temperature up to 15 K. This trend is best pronounced around 10 K, i.e., in the vicinity of the IC-C phase transition. The data suggest that additional interactions contribute to the magnon self-energy in the IC phase.

A possible qualitative explanation of this effect is that below T^* the wave vector \mathbf{k} is not a “good” quantum number of the magnon excitations. Magnons, specified by the

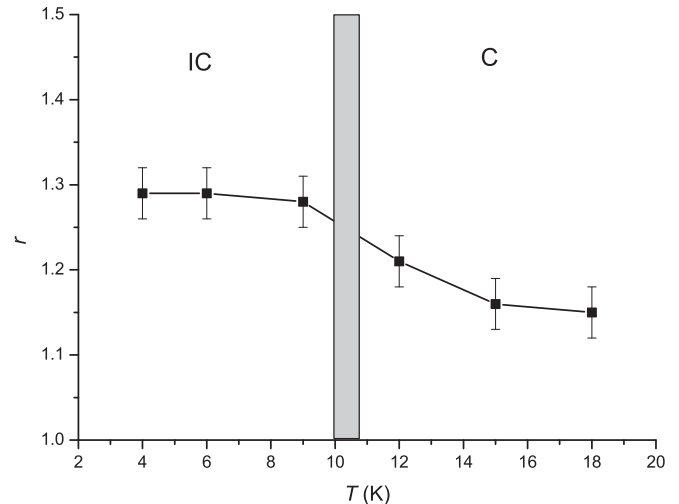


FIG. 7. Temperature dependence of the renormalization coefficient r in the vicinity of IC-C phase transition. The solid line is a guide for the eye.

dispersion relation (4), relax through scattering into states of wave vectors $\mathbf{k} \pm \mathbf{q}$ where \mathbf{q} is the propagation vector of the helimagnetic structure. Additionally, scattering from magnetic solitons¹ formed around T^* may also contribute to the magnon renormalization.

IV. SUMMARY AND CONCLUSIONS

Most of the Γ -point Raman-active phonons in CuB_2O_4 are identified and their symmetries are determined on the basis of polarized Raman measurements and first-principles DFT calculations. The TO-LO splitting of some of the B_2 modes has been observed and quantified. The phonon Raman spectra do not display resonant behavior in the visible spectral range.

The polarization selection rules and line-shape analysis allow us to assign the broad band centered at $\omega_0 = 82$ cm^{-1} to a two-magnon Raman process from the Cu(A) sublattice. The experimental band profile is described to a great precision within a model of interacting magnons and unequivocally confirms the suggested Fleury-Loudon mechanism of spin-light coupling, as well as the magnon dispersion relations studied earlier theoretically and experimentally by INS. An exchange interaction of 33 cm^{-1} between nearest-neighbor Cu(A) atoms is estimated from the Raman spectra, which corroborates the results of other experimental techniques.

Although the spectral shape of the $\omega_0 = 82$ cm^{-1} band displays no apparent discontinuities upon crossing the C-IC transition temperature, the quantitative line-shape analysis evidences detectable magnon self-energy effects in the IC phase. We hypothesize that the additional contribution to the magnon self-energy is a result of the magnon \mathbf{k} -vector relaxation due to scattering from the helimagnetic spin lattice, as well as from magnetic solitons, which are present at temperatures around T^* .

ACKNOWLEDGMENTS

This work is supported in part by the State of Texas through the Texas Center for Superconductivity at the University of

Houston and by International Travel Grant of the American Physical Society as well the Contract No. DRNF 02/1 of the Bulgarian National Science Fund. Three of the authors (V.G.I.,

M.V.A., and N.D.T.) would like to acknowledge the financial support of the Scientific Fund of the Sofia University through Contract No. 30/2013.

*vgi@phys.uni-sofia.bg

¹B. Roessli, J. Schefer, G. A. Petrakovskii, B. Ouladdiaf, M. Boehm, U. Staub, A. Vorotinov, and L. Bezmaternikh, *Phys. Rev. Lett.* **86**, 1885 (2001).

²M. Saito, K. Ishikawa, K. Taniguchi, and T. Arima, *Phys. Rev. Lett.* **101**, 117402 (2008).

³M. Saito, K. Ishikawa, S. Konno, K. Taniguchi, and T. Arima, *Nat. Mater.* **8**, 634 (2009).

⁴G. Petrakovskii, D. Velikanov, A. Vorontinov, A. Balaev, K. Sablina, A. Amato, B. Roessli, J. Schefer, and U. Staub, *J. Magn. Magn. Mater.* **205**, 105 (1999).

⁵M. Boehm, B. Roessli, J. Schefer, A. S. Wills, B. Ouladdiaf, E. Lelièvre-Berna, U. Staub, and G. A. Petrakovskii, *Phys. Rev. B* **68**, 024405 (2003).

⁶A. Pankrats, G. Petrakovskii, V. Tugarinov, K. Sablina, L. Bezmaternykh, R. Szymczak, M. Baran, B. Kundys, and A. Nabialek, *J. Magn. Magn. Mater.* **300**, e388 (2006).

⁷Toshiyuki Fujita, Yoshikuni Fujimoto, Seitaro Mitsudo, Toshihisa Idehara, Teruo Saito, Yusuke Kousaka, Shin-ichiro Yano, Jun Akimitsu, Jun-ichiro Kishine, Katsuya Inoue, and Mitsuhiro Motokawa, *J. Phys. Soc. Jpn.* **77**, 053702 (2008).

⁸M. Boehm, S. Martynov, B. Roessli, G. Petrakovskii, and J. Kulda, *J. Magn. Magn. Mater.* **250**, 313 (2002).

⁹S. Martynov, G. Petrakovskii, and B. Roessli, *J. Magn. Magn. Mater.* **269**, 106 (2004).

¹⁰CRYALISPRO, Agilent Technologies UK Ltd., 2010.

¹¹G. M. Sheldrick, *Acta Crystallogr., Sect. A: Found. Crystallogr.* **64**, 112 (2008).

¹²M. Martinez-Ripoll, S. Martinez-Carrera, and S. Garcia-Blanco, *Acta Crystallogr., Sect. B: Struct. Crystallogr. Cryst. Chem.* **27**, 677 (1971).

¹³G. K. Abdullaev and K. S. Mamedov, *Zh. Strukt. Khim.* **22**, 184 (1981) [*J. Struct. Chem.* **22**, 637 (1981)].

¹⁴J. P. Perdew, K. Burke, and M. Ernzerhof, *Phys. Rev. Lett.* **77**, 3865 (1996).

¹⁵S. J. Clark, M. D. Segall, C. J. Pickard, P. J. Hasnip, M. J. Probert, K. Refson, and M. C. Payne, *Z. Kristallogr.* **220**, 567 (2005).

¹⁶H. J. Monkhorst and J. D. Pack, *Phys. Rev. B* **13**, 5188 (1976).

¹⁷K. Refson, P. R. Tulip, and S. J. Clark, *Phys. Rev. B* **73**, 155114 (2006).

¹⁸E. Kroumova, M. I. Aroyo, J. M. Perez-Mato, A. Kirov, C. Capillas, S. Ivantchev, and H. Wondratschek, *Phase Transitions* **76**, 155 (2003); M. I. Aroyo, A. Kirov, C. Capillas, J. M. Perez-Mato, and H. Wondratschek, *Acta Crystallogr., Sect. A: Found. Crystallogr.* **62**, 115 (2006); M. I. Aroyo, J. M. Perez-Mato, C. Capillas, E. Kroumova, S. Ivantchev, G. Madariaga, A. Kirov, and H. Wondratschek, *Z. Kristallogr.* **221**, 15 (2006).

¹⁹L. N. Bezmaternykh, A. M. Potsel'niko, E. A. Erlykova, and I. S. Édel'man, *Phys. Solid State* **43**, 309 (2001).

²⁰P. A. Fleury and R. Loudon, *Phys. Rev.* **166**, 514 (1968).

²¹C. M. Canali and S. M. Girvin, *Phys. Rev. B* **45**, 7127 (1992).

²²A. V. Chubukov and D. M. Frenkel, *Phys. Rev. B* **52**, 9760 (1995).

²³F. J. Dyson, *Phys. Rev.* **102**, 1217 (1956); **102**, 1230 (1956).

²⁴S. V. Maleev, *Zh. Eksp. Teor. Fiz.* **30**, 1010 (1957) [*Sov. Phys.-JETP* **6**, 776 (1958)].